Nanoscale

Accepted Manuscript

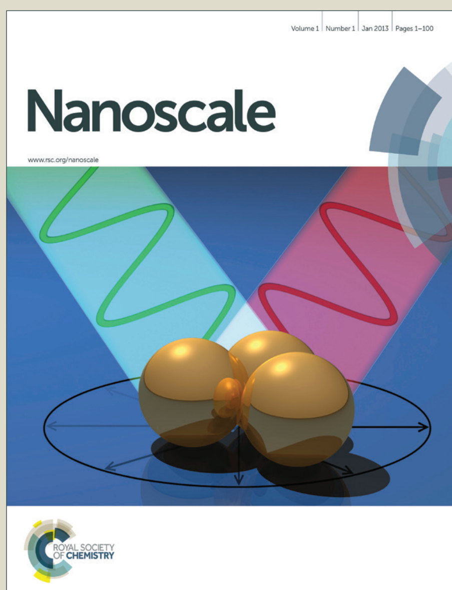

This is an *Accepted Manuscript*, which has been through the Royal Society of Chemistry peer review process and has been accepted for publication.

Accepted Manuscripts are published online shortly after acceptance, before technical editing, formatting and proof reading. Using this free service, authors can make their results available to the community, in citable form, before we publish the edited article. We will replace this *Accepted Manuscript* with the edited and formatted *Advance Article* as soon as it is available.

You can find more information about *Accepted Manuscripts* in the Information for Authors.

Please note that technical editing may introduce minor changes to the text and/or graphics, which may alter content. The journal's standard Terms & Conditions and the Ethical guidelines still apply. In no event shall the Royal Society of Chemistry be held responsible for any errors or omissions in this *Accepted Manuscript* or any consequences arising from the use of any information it contains.

ROYAL SOCIETY OF CHEMISTRY

www.rsc.org/nanoscale

Tunable surface plasmon resonance and enhanced electrical conductivity of In doped ZnO colloidal nanocrystals

Sirshendu Ghosh, Manas Saha and S. K. De*

Department of Materials Science, Indian Association for the Cultivation of Science, Kolkata-700032, India

Abstract: We report a new synthesis process of colloidal indium (In) doped zinc oxide (ZIO) nanocrystals by hot injection technique. By fine tuning of synthesis we reached the same nucleation temperature for indium oxide and zinc oxide which helped us to study a dopant precursor dependent In incorporation into ZnO matrix by taking different In sources. The dopant induced shape evolution changes the hexagonal pyramid structured ZnO to platelet like structure upon 8% In doping. Introduction of trivalent In^{3+} into ZnO lattice and consequent substitution of divalent Zn^{2+} generates free electrons in conduction band which produces a plasmonic resonance in the infrared region. The electron concentration controls plasmon frequency as well as band gap of host ZnO. The variation of band gap and the modification of conduction band have been explained by Burstein-Moss effect and Mie's theory respectively. In dopant changes the defect chemistry of pure ZnO nanocrystals which has been studied by photoluminescence and other spectroscopic measurements. The nanocrystals are highly stable in organic medium and can be deposited as a crack free thin film on different substrates. Careful ligand exchange and thermal annealing of spin cast film leads to well conductive film (720 Ω/sq to 120 Ω/sq) with stable inherent plasmonic absorption at infrared and 90% transmittance at visible region. Temperature induced metal-semiconductor transition was found for doped ZnO nanocrystals. The transition temperature shifts to lower temperature with increase of doping concentration.

* Corresponding author. Phone: +91-33-2473-3073. E-mail: msskd@iacs.res.in.

Nanoscale Accepted Manuscript

1. Introduction

The simultaneous appearance of optical transparency, optical absorption and electrical conductivity in the same material is very rare due to mutually exclusive phenomenon. Electronic energy band structure and carrier concentration are the key factors to combine such unique properties in wide band gap semiconductors. Transparent conductive oxides (TCO) belong to a class of material where high transmission in visible spectrum range and high electrical conductivity coexist. The TCOs have the increasing importance for more technological improvement of quality as well as efficiency of display panel and solar energy conversion devices.[1] The most technologically used and well documented TCOs are fluorine-doped tin oxide (FTO), antimony-doped tin oxide (ATO),[2] tin-doped indium oxide (ITO),[3] aluminium-doped zinc oxide (AZO),[4] gallium-doped zinc oxide (GZO),[5] indium doped zinc oxide (IZO),[6] indium doped cadmium oxide (ICO)[7] and niobium-doped TiO_2 (NTO).[8] In all these TCO's, large band gap n-type semiconducting oxides are turned into highly electrical conducting systems by doping with proper elements of higher valency. By controlling the carrier concentration, TCO can be easily converted to plasmonic material which may reveal strong optical absorption in desired wavelength region. Localised surface plasmon resonance (LSPR) in heavily doped degenerate semiconductor is also helpful in surface enhanced Raman scattering (SERS) application for biological species. The continuous increasing demand of TCOs in enlargement of display panel, improvement in sensitivity of photovoltaics for a wide spectral range of the sun and biological applications stimulated researchers to develop new TCOs with earth abundant elements by low cost processing technique.

The completely filled d orbital based TCO films (mainly ZnO and CdO) have proved excellent TCO characteristics in last few years.[9-12] Zinc Oxide (ZnO) is the most attractive

Nanoscale Accepted Manuscript

semiconductor due to wide direct band gap (~3.3 eV), high refractive index (1.99), large exciton binding energy (~60 meV) and simpler chemical synthesis method. Moreover, Zn is an earth abundant and low cost metal. Nanoforms of ZnO have already established its intriguing and exciting properties in luminescence performance, optoelectronic devices,[13] catalytic activity, SERS application[14] and also as a fascinating candidate in the class of TCO.[4] The aliovalent cations such as Group III elements (B,[15] Al, Ga and In) have been successfully doped into ZnO crystals which show good TCO behaviour.

Traditionally doped ZnO is directly synthesized in the form of thin films using various costly and complicated processes such as Chemical vapour deposition and physical vapour deposition like magnetron sputtering, vacuum evaporation and pulsed laser ablation. The major weaknesses of the above mentioned processes are the selection of suitable substrate structure, less control of growth and expensive equipments. Colloidal synthesis of nanocrystal is the most advantageous one as the process gives a broad window of opportunity to control the size, shape, doping percentage, high solubility in appropriate solvent (polar or nonpolar) and self-assembly. Moreover the colloidal nanocrystal offers a potential strategy for low cost deposition of TCO films over large area, patterned way (colloidal "Ink") or on specialised substrate (plastic, polymer substrate) at room temperature. So ZnO based TCO colloid is highly attractive due to easy preparation, lower cost and high abundance of zinc along with low toxicity.

In this article, we report for the first time the high yield synthesis of monodisperse In doped ZnO (ZIO) nanocrystals (NC) with high colloidal stability up to doping percentage of 8. The synthesis procedure involves in the thermal decomposition of Zn-carboxylate salt in the presence of oleylamine and oleic acid in nonpolar solvent. We exclusively studied the effect of In dopant precursors on doping amount within host ZnO matrix. By fine tuning of synthesis

Nanoscale Accepted Manuscript

condition we achieved the same nucleation temperature (T_{Nu}) for ZnO and In_2O_3 NCs for successful doping at low dopant budget. The incorporation of In^{3+} as a dopant leads to appearance of tunable broad absorption peak at near infrared (NIR) region. From spectroscopic analysis we tried to explain the change in band structure of ZnO upon doping. In^{3+} incorporation in ZnO matrix has an effect of evolving the shape of the ZIO nanocrystals. They transform progressively from perfect pyramidal structure to reduced pyramid and finally to hexagonal platelets (Scheme-I).

2. Experimental Section

Materials: All chemicals purchased from various manufacturers were used directly without further purification. Zinc acetylacetonate [$Zn(acac)_2$, 99%], Indium acetylacetonate [$In(acac)_3$, 99%], Indium acetate [$In(OAc)_3$,99.99%] and 1-octadecene [ODE, 90%] were purchased from Alfa Aeser. Oleic acid [(OLAH), 99%], Oleylamine [(OLAM) 70%, tech] and tetrachloroethylene (TCE) were purchased from Aldrich. Formic acid (GR), acetonitrile (GR), ethyl alcohol (GR), acetone (GR), n-octane and n-hexane (GR) were purchased from Merck. All synthetic experiments were conducted using a schlenk line under a dry Ar atmosphere.

Synthesis: In a typical synthesis, 1 mmole of $Zn(acac)_2$ was mixed with 2 mmole of OLAH and 5 ml of ODE in a 25 ml three neck round bottom flask fitted with a reflux condenser. The mixture was initially vacuumed to remove dissolved gases at room temperature and was further heated to 90 °C under dynamic vacuum condition for 15 mins. Thereafter the total system was backfilled by purging dry Ar and maintained a continuous flow of Ar till the end of reaction. At this stage 15 mmole OLAM dissolved in 1 ml ODE was injected to reaction flask. The transparent yellow solution was heated to 240 °C at a heating rate of 10 °C/min. The reaction

Nanoscale Accepted Manuscript

was continued at this temperature for 60 mins to obtain nearly monodisperse colloidally stable ZnO nanopyramids. The reaction mixture was cooled to room temperature and 5 ml of n-hexane was added. The nanopyramids were precipitated by addition of excess ethanol as non solvent. The as prepared product was collected by centrifugation at 8000 rpm for 5 mins. This washing process was repeated several times to remove impurities. The as formed nanopyramids were very soluble in non polar solvents such as hexane, toluene or TCE etc.

For synthesis of In doped ZnO ($Zn_{1-x}In_xO$) NC, indium source was introduced in different molar ratio with Zn source to prepare 1 mole% ($ZnIn_1$), 2 mole% ($ZnIn_2$), 4 mole% ($ZnIn_4$), 6 mole% ($ZnIn_6$) and 8 mole% ($ZnIn_8$) In^{3+} doped samples keeping all the reaction conditions similar.

Characterization: Fourier transform infrared (FT-IR) spectra of the samples were taken by using a Perkin Elmer spectrochem 100 FT-IR spectrometer. The crystalline phases of the products were determined by X-ray powder diffraction (XRD) by using Bruker AXS D8SWAX diffractometer with Cu K_α radiation (λ= 1.54 Å), employing a scanning rate of 0.5° S^{-1} in the 2θ range from 20° to 80°. For XRD measurement the hexane solution of the NCs was drop cast over amorphous silicon sample holder till a naked eye visible thin layer was formed. Transmission electron microscopy (TEM) images, high angle annular dark field scanning TEM (HAADF STEM) images and energy dispersive spectrum (EDS) were taken using an Ultra-high resolution field emission gun transmission electron microscope (UHR-FEG TEM, JEM-2100F, Jeol, Japan) operating at 200 kV. For the TEM observations, the sample dissolved in hexane was drop cast on a carbon coated copper grid. The morphologies of the samples and film thickness were studied by a field emission scanning electron microscope (FESEM, JEOL, JSM 6700F). The dopant percentage was determined by inductively coupled plasma (ICP) using Perkin – Elmer Optima

Nanoscale Accepted Manuscript

2100 DV machine. For ICP measurements at first the purified NCs were digested in concentrated HNO_3 and the resultant solution was diluted to a proper degree with mili-Q water. The room temperature optical absorbance of the samples was recorded by a Varian Cary5000 UV-VIS-NIR spectrophotometer. Photoluminescence (PL) measurements were carried out at room temperature with a Fluorescence spectrometer (Hitachi, F-2500). Valence state analysis was carried out by using an X-ray photoelectron spectroscopic (XPS, Omicron, model: 1712-62-11) method. XPS measurement was done using an Al-Kα radiation source under 15 kV voltage and 5 mA current. For XPS measurement the hexane solution of the NCs was drop cast over glass slide (2mm × 2mm) till a naked eye visible thin layer was formed.

Thin flim preparation and Electrical measurements:

A 2×2 cm^2 large quartz substrate was first washed with deionized (DI) H_2O and ethanol, and then dried in N_2 at 120 °C for 12 hrs. A total of 0.2 ml of the NC solution in mixed solvent (n-hexane: n-octane = 1:1, solution concentration = 30mg/ ml) was spin casted onto the glass substrate at 800 rpm for 60 secs and dried under vacuum at 80 °C for 1 hr. Then the film was immerged in formic acid solution in acetonitrile to exchange the long chain ligand with formic acid for 5 mins. The ligand exchanged film was annealed at 300 °C for 2 hrs in dry Ar atmosphere. The annealed film was used for electrical conductivity measurements. Aluminium conducting pad was deposited on two sides of film by thermal evaporation to make good electrical contact using Ag paste. The resistivity of the samples was measured at temperature range 80 K to 300 K using Keithley Elcetrometer 6517A and Lakeshore temperature controller model 332.

3. Results and Discussion:

Nanoscale Accepted Manuscript

The highly colloidal stable monodispersed In doped ZnO NCs were synthesized by thermal decomposition of organometalic precursor in a nonpolar solvent ODE. The nucleation temperature (T_{Nu}) of ZnO NC is highly dependent on the decomposition temperature of organozinc precursor and rate of nucleophilic attack of amine (or accelerating agent) to the precursor. For successful doping in ZnO NCs, the host precursor and the dopant precursor should decompose at more or less same temperature. The nucleation temperature (T_{Nu}) for ZnO NCs was found to be 240 °C which was concluded from temperature dependence absorbance spectra and TEM image (See ESI, Fig. S1 and S2). When $Zn(acac)_2$ (1 mmole) is mixed with OLAH (2 mmole) in ODE solvent and vacuumed continuously at 90 ^{0}C , it results in the formation of $Zn(acac)_{2-x}(OLA)_x$ intermediate complex (details in ESI, Fig. S3). Injection of degassed OLAM in excess (15 mmole) to this intermediate complex dissolved in ODE results in the nucleation of ZnO nuclei at 240 °C (See ESI, Fig. S1, S2). Stronger binding of OLA^- ligand compare to $acac^-$ ligand to Zn^{2+} centre is the main reason for higher temperature nucleation of ZnO (formation of ZnO NCs was found at 200 °C when OLAH was not used). We took different In^{3+} sources of same mole % namely $In(OAc)_3$ and $In(acac)_3$ to test maximum In^{3+} incorporation in identical reaction conditions. Table 1 shows the indium percentage estimated from ICP and EDS analysis of ZnIn NCs by taking different In^{3+} sources as starting material. It is found that larger amount of In^{3+} ions are incorporated in host matrix for $In(acac)_3$ rather than $In(OAc)_3$. The formation of In_2O_3 from $In(OAc)_3$ and $In(acac)_3$ precursors in the same chemical environment as evidence from TEM (ESI, Fig. S5 and S6) indicates that the formation of In_2O_3 initiate at 290 °C and 240 °C which results from the decomposition of $In(OAc)(OLA)_2$ and $In(acac)(OLA)_2$ intermediates respectively(See ESI Fig. S7). Precursor dependent nucleation and subsequent growth of ZnO and In_2O_3 NCs has been observed from TEM images with time. (ESI, Fig.S2,S5 and S6). Time

Nanoscale Accepted Manuscript

dependent absorption spectra (ESI, Fig. S13) indicate that In is incorporated in ZnO in initial stage (5 sec) of the reaction.

Fig. 1a shows the XRD pattern of as prepared ZnIn NCs doped up to 8 mole% of Indium in ZnO matrix. The diffraction peaks are readily indexed to würzite type ZnO (JCPDS No: 36-1451) for pure and doped ZnO. The würzite type ZnO has hexagonal structure with C_{6v}^{4} space group ($P6_{3mc}$). No other oxide based crystalline impurities such as Indium oxide (In_2O_3) or mixed oxide ($ZnIn_2O_4$) which is very common in In doped ZnO thin films were not found.[16,17] It has been observed that Bragg peaks are broadened with increase of concentration of In, might be a result of coherent length in nanoscale region and acquire in lattice strain. Generally compression or elongation of bonds between the atoms develops the lattice strain which gives rise to the change of spaces of crystallographic planes. In^{3+} is a larger ion (r_{ionic}=0.094 nm) than the Zn^{2+} (r_{ionic}=0.074 nm), so the successful incorporation of In^{3+} in lattice should cause the expansion of lattice and generation of tensile strain. The most intense diffraction peaks such as (100), (002) and (101) are shifted towards lower angle (2θ) which confirms the presence of tensile strain.

Rietveld analysis (ESI, Fig. S8a) was carried out using software Maud (http://www.ing.unitn.it/~maud/) by refining structural and micro structural parameters to estimate the lattice parameters (a and c), cell volume (V) and inhomogeneous tensile strain. Fig. 1b displays the expansion (%) of lattice parameter a and c with In^{3+} concentration (%). Both a and c values increase with increasing In^{3+} load in ZnO which demonstrates the successful incorporation of dopant in lattice site. We found the solid solution limit of In^{3+} in ZnO is 8 mole% in our synthesis protocol. The tensile strain (Fig. 1b) also increases with higher loading percentage of In^{3+}. A non-linear increase of tensile strain and lattice parameters with increase of

Nanoscale Accepted Manuscript

In^{3+} concentration is observed. This may be due to the imperfect comparison between pure and doped NCs which are not exactly the same size. Furthermore incorporation of dopant ion in interstitial position may result in non-linear trend. Unit cell volume (V) was calculated by using the following equation:

$$V = 0.866 \times a^2 \times c \quad (1)$$

The value of V changes from 44.61 Å^3 to 45.86 Å^3 with increase of In^{3+} doping concentration (ESI, Fig. S8b). The variation of V with In^{3+} concentration follows the non-linear trend.

Fig. 2a displays the representative field emission scanning electron microscopy (FE-SEM) image of pure ZnO NC. The transmission electron microscopic images at low magnification (Fig. 2b) reveal that hexagonal pyramid shaped ZnO NCs with an average size of 40 nm width and 35 nm height were produced. The top-left and bottom-right insets of Fig. 2b depict the tilted ($X = 41.1°$, $Y = 0°$) and side views of a single ZnO hexagonal nanopyramid. The calculated angle between two opposite edges at the tip of the pyramid is 62°, and the angle between the edge and the basal plane is 59° as indicated in Fig. 2b. The well defined diffraction spots are indexed to the hexagonal würzite structure (Fig. 2c) consistent with the XRD data. Fig. 2d shows a single hexagonal pyramid viewed from top which also confirms hexagonal nature of the base of NC. Fig. 2e depicts the corresponding selected area electron diffraction (SAED) pattern of the NC which can be indexed as diffractions from [0001] zone axis. The indices of diffraction spots imply that side surfaces of hexagonal pyramid are surrounded by $\{10\bar{1}0\}$ planes. From SAED pattern and the angle between the edge and basal planes (~ 59°) of the NC, we conclude that the exposed six surfaces are $\{10\bar{1}1\}$ facets. Fig. 2f gives a schematic view of a complete ZnO hexagonal pyramid. The würzite structured ZnO crystal is generally described

Nanoscale Accepted Manuscript

schematically as combination of alternating planes constituted of fourfold tetrahedrally co-ordinated Zn^{2+} and O^{2-} ions, staking alternatively along the c axis.[18] The Zn^{2+} cations rich plane and O^{2-} anions rich plane form positively charged (0001)-Zn and negatively charged $(000\bar{1})$-O polar surfaces respectively. These two oppositely polar surfaces generate a permanent and spontaneous dipole moment along the c axis and tend to diverge the surface energy.[19,20] Normally most of the ZnO nanostructures grow along the c axis i.e. along the [0001] direction with exposing the six nonpolar $\{10\bar{1}0\}$ facets which is parallel to [0001] direction, the polar {0001} and $\{000\bar{1}\}$ planes.[21] The nonpolar $\{10\bar{1}0\}$ facets are more stable than the parallel polar {0001} and $\{000\bar{1}\}$ facets due to the lower surface energy of former one.[22] Besides these two polar surfaces, ZnO has other typical polar surface $\{10\bar{1}1\}$.[23] During the growth of ZnO nanostructures usually $\{10\bar{1}0\}$ and $\{2\bar{1}\bar{1}0\}$ nonpolar surfaces are the large facets with preferential growth along the c axis rather than polar {0001} surfaces. In our as synthesized ZnO nanopyramid, polar $\{10\bar{1}1\}$ facets were the more exposed surface than the nonpolar $\{10\bar{1}0\}$ facets although the later facets are thermodynamically more stable.[24] The thermodynamically unstable facets become the more exposed faces due to the predominating kinetic control of reaction system during the growth process. The high energy $\{10\bar{1}1\}$ facets are stabilised by proper surface capping of organic molecule which favours the crystal termination on the $\{10\bar{1}1\}$ by diminishing the surface energy. The capping molecules compensate the surface charge by the strong electrostatic interaction between the polar surfaces and polar head of capping molecule. Thus the surface energies of basal polar {0001} planes and polar $\{10\bar{1}1\}$ planes may decrease in comparison with those other nonpolar faces resulting in a comparatively slow growth rate for these polar planes.

Nanoscale Accepted Manuscript

To understand the exact effect of capping molecule on modification of surface polarity and stabilisation of a particular growth surface, we varied the reaction condition to detect the change in morphology of product. Fig. S9 demonstrates the FTIR spectra of as synthesized ZnO and OLAM. The band at 3342 cm^{-1} in the IR spectrum of OLAM is due to the N-H stretching mode, which is red shifted and highly broadened at 3436 cm^{-1} in OLAM capped ZnO NC due to the absorption of N-H groups onto the ZnO surface. The peak at 1583 cm^{-1} for NH_2 scissoring mode is red shifted to 1596 cm^{-1} and also broadened.[25] An increase in intensity and broadening of C-N stretching band at 1058 cm^{-1} confirm the complete surface protection by OLAM. Although amide was a by product in synthesis, as no peak corresponding to amide group was found in IR spectra of as synthesized ZnO, we can conclude only the amine took part in surface capping not the amide or acid group.

When OLAM was injected at 240 °C instead of very beginning of reaction (90 °C) to the reaction solution containing Zn-source and OLAH, the resulted product after 60 mins of reaction is hexagonal platelets with irregular size and shape instead of hexagonal nanopyramid which are depicted in Fig. S10. So OLAM might participate in growth of $\{10\bar{1}1\}$ surface. The FT-IR spectra of $Zn(acac)_2$ and OLAM heated at 90°C are demonstrated in Fig. S3b, which shows that the symmetric and antisymmetric COCC stretching vibrations of $Zn(acac)_2$ at 1578 cm^{-1} and 1517 cm^{-1} are red shifted.[26] This can be due to the formation of $Zn(acac)_2$-OLAM complex and the donor NH_2 group sharing its lone-pair of electrons with the Zn^{2+} ions. But when OLAM is added at T_{nu} rapid nucleophilic attack of NH_2 takes place at carbonyl centre rather than coordination with Zn^{2+} ions, results in rapid growth along stable nonpolar $\{10\bar{1}0\}$surfaces. Due to the lower monomer concentration of nuclei and rapid surface protection by OLAM, platelet structure is formed rather than preferential growth along the c axis. Addition of OLAM at low

Nanoscale Accepted Manuscript

temperature leads to consumption of some amount of OLAM by coordination with Zn^{2+} in intermediate complex, which gives rise to slow decomposition of the complex and control growth rate of polar $\{10\bar{1}1\}$ surfaces. High monomer concentration prefers growth along the c axis. So slow growth rate of ZnO and proper capping by OLAM lead to the formation of beautifully synthesized nanopyramid.

Fig. 2g shows the UHRTEM image of a NC captured at the cross-section of two basal edges, which shows surface termination at basal side by $(11\bar{2}0)$ and $(01\bar{1}0)$ planes and presence of $(10\bar{1}0)$ planes parallel to basal edges. The inset at left top depicts the FFT pattern of the corresponding area, which demonstrates the direction of $(11\bar{2}0)$ and $(01\bar{1}0)$ planes i.e.; $[11\bar{2}0]$ and $[\bar{1}2\bar{1}0]$, makes a cross sectional angle of 120° (also it is the angle between two basal edge). The FFT pattern also shows the presence of $(10\bar{1}0)$ planes. Fig. 2h shows the side view of ZnO NC where the blue and red squared areas are the tip and base of pyramid. HRTEM images of both the area (Fig. 2i and 2j) depict the presence of mutually perpendicular $(10\bar{1}0)$ and (0002) planes (the zone axis is $[11\bar{2}0]$). It is found that the *d* value of (0002) plane is nearly doubled at base, which is probably due to the high thickness of base; Moiré pattern of crystalline plane is appearing.

Figs. S11a to S11c show the TEM images for the $ZnIn_2$, $ZnIn_4$ and $ZnIn_6$. Whereas Fig. S12 depicts the TEM images of $ZnIn_8$ NC. It is observed that the pyramid height gradually decreases from 35 nm to 11 nm on increasing the In^{3+} content leading to the formation of hexagonal platelets. Incorporation of In^{3+} into ZnO crystal lattice increases the surface polarity of Zn rich polar surfaces, i.e.; Zn-$\{0001\}$ and Zn-$\{10\bar{1}1\}$ surfaces due to higher electronegativity of In^{3+} than Zn^{2+}. This accretion of surface polarity favours faster electrostatic interaction and consequent surface stabilisation or capping by OLAM onto the Zn-$\{0001\}$ and Zn-$\{10\bar{1}1\}$

Nanoscale Accepted Manuscript

surfaces. More In^{3+} loading leads to more charge accumulation on described surfaces which results in quenching of growth along the c-axis (decrease in pyramid height) and less exposure of $\{10\bar{1}1\}$ surfaces. At 8% of In^{3+} doping only the hexagonal platelet is formed where $\{10\bar{1}1\}$ surface no more exists. Change of basal length is negligible compare to the change of height.

Several studies indicate that dopant ions significantly influence nucleation and growth of NCs during synthesis.[27-29] Types of doping i.e. nucleation doping or growth doping depend on growth rate, residence time, morphology and crystal structure.[30] Generally, the nucleated NCs exclude dopant ions from the internal crystal lattice to the surfaces of NCs. Synthetic method in other words growth kinetics limits the maximum doping concentration in colloidal semiconductor NCs. Moreover dopants change the free energy for the stabilization of host crystal structure due to incompatibility in crystal structure and chemical property.[31] Identical decomposition temperature of in-situ formed $Zn(acac)_{2-x}(OLA)_x$ and $In(acac)(OLA)_2$ precursors and the fast growth rate lead to maximum In incorporation into ZnO NCs. TEM measurements indicate that the size of NC decreases with increase of doping concentration. Thus In dopant ions introduce a thermodynamic potential barrier around the doped ZnO NCs to inhibit NC growth. Internal lattice strain controls the solubility of NCs as described by Gibbs-Thomson relation[27]:

$$S_r = S_B \exp[2\sigma V_m / rRT] \qquad (1)$$

Where S_r is the solubility of the crystallite of radius r, S_B is the solubility of corresponding bulk material, V_m is the molar volume, σ is the specific surface energy of nanocrystals. Lattice strain increases continuously with increase of In concentration. Equation (1) suggests that larger strain induces greater crystallite solubility. As a result of it In dopants inhibit the growth of ZnO NCs.

Nanoscale Accepted Manuscript

To further elucidate the doping status and distribution of In^{3+} in ZnIn NCs, systematic characterisations including energy dispersive X-ray spectroscopy (EDS) element mapping and X-ray photoelectron spectra (XPS) were performed. The EDS element mapping of 4% In doped ZnO NCs was carried out to determine the exact position and spatial distribution of dopant ions in the NCs. Fig. 3 shows the HAADF-STEM image of large number of $ZnIn_4$ NCs which clearly indicate incomplete pyramidal nature of NCs. The EDS element mapping of large number of NCs (in fig. 3) shows that In^{3+} ions are homogeneously distributed among the NCs. No phase separation or agglomeration was noticed which concludes that the dopant distribution is quite good. Other two elements Zn and O are also present in nearly stoichiometric ratio and in well distribution. However, the EDS element mapping results cannot verify that the In^{3+} ions are located in NCs or on the surface of ZnIn NCs. So fourth, XPS measurements were carried out to further investigate the exact position and binding modes of In^{3+} and other elements.

Fig. 4 displays the fine scanned Zn2p, O1s and In3d peaks of pure and 4% In doped ZnO samples. The binding energies of Zn $2p_{1/2}$ and $2p_{3/2}$ are around 1047.98 eV and 1024.91 eV respectively with spin-orbit splitting of 23.07 eV for pure ZnO NCs (Fig. 4a). From the binding energy position, observed spin-orbit splitting value and the highly symmetric nature of high intense peaks, it concludes the presence of Zn as only in the +2 oxidation state in würzite ZnO crystal.[32] The shift of Zn 2p peaks in $ZnIn_4$ sample toward the lower energies is due to the partial substitution of lattice Zn by In^{3+} ions in ZnO and formation of Zn-O-In bonding interaction. Indium is supposed to be present mostly as In^{3+} which forms a strong covalent bond with O^{2-} in doped nanocrystals. Such a strong covalent effect weakens the neighbouring Zn-O bonds and results in decrease of relative positive charge density on Zn ions which causes diminishment of binding energy of Zn 2p peaks. Moreover, the Zn-In interaction i.e. Zn-In bond formation in

Nanoscale Accepted Manuscript

würzite ZnO may cause a decrease in binding energy of Zn^{2+} 2p peaks due to smaller difference of electro-negativity between Zn and In compare to Zn and O ($\Delta\varkappa_{Zn\text{-}In}$ = 0.1, whereas $\Delta\varkappa_{Zn\text{-}O}$ =1.6, according to Pauling scale).[33] The broadening of peaks is a result of reduced crystalline size and surface plasmon which increases free electron concentration on nanocrystal surface. Fig. 4b demonstrates the O 1s peak of both doped and undoped ZnO NCs. Deconvolution of broad O 1s peak through Peak fit analysis results in a major peak and a sub peak at 533.45eV and 534.81 eV respectively. The lower energy peak is attributed to the O^{2-}ions in the würzite structure of the hexagonal Zn 2þ ion array. Therefore, the lower energy peak of oxygen spectrum can be attributed to Zn-O bonds.[34] The peak at 534.81 eV is attributed to O^{2-} ions in oxygen deficient regions and is related to the presence of oxygen vacancy (V_o).[35] The O 1s peak for $ZnIn_4$ samples is quite broad and inhomogeneous nature compare to pure one. Deconvolution of fitted curve gives three peaks at 534.35 eV, 532.77 eV and 530.16 eV. Both the crystallite O^{2-} peak and oxygen vacancy related peaks at 532.77 eV and 534.35 eV respectively are significantly broader than that for pure one. Formation of In-O covalent bond changes the effective electric charge on O anion, and the broadness is a mixed effect from In-O and Zn-O bond formation. Large area of the peak related to V_o in doped NCs reflects the increase in oxygen vacancy concentration on the nanocrystals surface during the doping. A new hump like peak is appeared at lower energy (530.16 eV) in $ZnIn_4$ NCs which indicates the presence of oxygen interstitials (O_i).[36] Fig. 4c shows the XPS characteristics peaks for In^{3+}. Two major peaks at 454.51 eV and 446.86 eV are appeared for $In3d_{3/2}$ and $In3d_{5/2}$ spin-orbit coupling states which is in a very good agreement with the presence of In dopant as In^{3+} ion in würzite matrix.[37] Both the peaks somewhat broad and little asymmetric in nature, possibly due to the presence of In^{3+} in both in the bulk lattice site and

Nanoscale Accepted Manuscript

surface site. Sharp and smooth natures of In3d peaks also indicate the presence of appreciable amount of In^{3+} on the surface of NCs.

We carried out absorption spectroscopy to assess the influence on doping to increase the free electron concentration hence change in electronic energy band structure of n-type ZnO host matrix. Fig. 5 shows the absorption spectra of doped and pure ZnO NCs dissolved in TCE in the wavelength range of 300 nm to 3000 nm. All the doped NCs show two strong absorption bands one at UV region and another at near infrared (IR) region. The broad featureless band at IR region can be attributed to surface plasmon absorption of doped NC. The surface plasmon energy decreases with increase of the effective refractive index of the sample by the addition of high refractive index solvent. (Fig. S22) The plasmonic absorbance at IR region is confirmed by the observation of shifting of plasmonic band with solvent variation. The excess electron created in the system due to n-type doping can resonance in the confined dimension of NC. The resonance excitation of this plasmon by electromagnetic radiation results in the absorbance at IR region. The IR absorption intensity increases monotonically with the increase of In^{3+} doping concentration. We cannot collect the absorbance nature beyond 3000 nm for the instrument limitation and appearance of noise due to the vibrational overtones of solvent molecules. To get the clear nature of IR absorbance by NCs, we performed FT-IR spectroscopy with the powdered sample which will be discussed in later paragraph.

The plasmon band appeared at IR region is an effect of presence of free electrons in the conduction band. The modified Drude-Lorentz model can quantitatively explain this phenomenon.[38] According to this model there is a direct proportional relationship between the absorption coefficient (α) of free electron in semiconductor and the charge carrier density (N) as follows:

Nanoscale Accepted Manuscript

$$\alpha = \frac{e^2 N}{m^* \varepsilon_0 n c \tau \omega^2} \quad (2)$$

where c and ω are the speed and frequency of incident light, e is the electron charge, m^* is the effective mass of an electron, ε_0 is the vacuum permittivity, τ is the mean time between two electron scattering events, n is the refractive index of pure semiconductor. Furthermore according to Mie's theory,[39] the energy position of plasmon band is related to the surface plasmon resonance frequency (ω_p) which is proportional to the square root of the free electron concentration:

$$\omega_p = \sqrt{\frac{Ne^2}{m^* \varepsilon_{opt} \varepsilon_0}} \quad (3)$$

Where ε_{opt} is the dielectric constant measured in the transparent region of the spectrum of a pure semiconductor sample. It is very clear from the nature of IR absorbance of samples as depicted in Fig. 5 that the plasmon band absorption maximum (normalised with respect to band gap absorbance) increases with increasing of In^{3+} doping concentration due to gradual increase of free electron concentration, also quite expected according to equation (2). The IR absorbance of $ZnIn_8$ NC (in Fig. 6) is found to be broader compare to other doped NC along with reduction in absorbance intensity compare to $ZnIn_6$ (Fig. 5). This behaviour may be a result of inhomogeneous doping, electron trapping around In^{3+} sites[40] and destruction of particle size distribution. Fig. 6 shows the change of plasmon band energy with the variation of In^{3+} doping concentration. The broad surface plasmon resonance peak shifts to higher energy on increasing doping concentration suggesting an increase in the amount of free carriers. Based on equation (3) and taking the optical parameter values ($m^* = 0.24\ m_0$ and $\varepsilon_{opt} = 7.77$) for bulk würzite ZnO system,[41] the concentration of free electron is found to be 6.491×10^{19} cm^{-3}, 8.476×10^{19} cm^{-3} , 9.22×10^{19} cm^{-3}, 11.092×10^{19} cm^{-3} and 14.069×10^{19} cm^{-3} for 1%, 2%, 4%, 6% and 8% In^{3+} doped

Nanoscale Accepted Manuscript

NCs respectively. These values are comparable with previous reported values for In or Ga doped ZnO films.[42,43] The change of plasmon energy and free electron concentration are in agreement with Drude's model for the free electron gas formation in semiconductors.

Besides the modification of surface plasmon resonance in IR region there is a continuous change of band gap of ZnIn NC. The optical band gap of ZnIn NC with different In loading was determined from differential absorbance spectra (dA/dλ *vs.*λ)[44] shown in Fig. S14. A progressive blue shift of band gap is observed on increasing doping percentage. Introduction of In^{3+} dopant into the ZnO matrix creates free electrons which generally accumulate at the bottom of conduction band resulting in an increase of band gap. This phenomenon is known as Burstein-Moss (BM) effect.[45-47] As our synthesized NCs are not in quantum confinement region so the amplification of band gap is solely attributed to the BM effect. The resulting band gap from derivative plot is summarised in Table 2 which shows an increase of band gap from 3.395 eV (for pure one) up to 3.576 eV (for $ZnIn_6$ NCs). The increase in the Fermi level in the conduction band of the degenerate semiconductor leads to an energy gap widening effect. According to the BM effect, broadening of the optical band gap can be expressed as follows:[48]

$$\Delta E^{BM} = \frac{\hbar 2}{2\mu}(3\boldsymbol{\pi}2\mathrm{N})^{2/3} \quad (4)$$

Where $\frac{1}{\mu} = \frac{1}{m_h^*} + \frac{1}{m_e^*}$

In which ΔE^{BM} is the energy band gap broadening, $\hbar$ is the reduced Planck constant, μ is the effective mass of the carrier, N is the carrier concentration, m_h^* and m_e^* are the effective mass of hole and electron with the value $0.28m^0$ and $0.59\ m^0$ (m^0 = free electron mass) respectively.[49] According to this equation band gap increases with carrier concentration. The electron concentration (N) calculated from equation (4) for different In^{3+} concentrations is summarised in

Nanoscale Accepted Manuscript

Table 2. The N values calculated from equation (4) are very similar to that found using Mie's theory where ω_p is the experimental quantity. It suggests that doping process is very homogenous and might create similar effect on band gap and plasmonic frequency enhancement. The little lower value in magnitude of N using BM effect is found probably due to the negligence of dielectric constant of medium. There is a decrease in band gap as well as electron concentration (calculated from BM effect) for $ZnIn_8$ compare to $ZnIn_6$. At higher concentration of doping, In^{3+} introduces some localised states of energy into the ZnO band structure which can interact with conduction band. This interaction leads to mixing and anticrossing of these bands which results a gap in the conduction band with perturbed bands of energy (destruction of parabolic nature of conduction band). Therefore, the magnitude of the E_g is reduced when the optical transition promotes electrons from the valence band to states in the conduction band close to the new gap (Scheme II C).[50,51] Even at higher doping concentration ca. 6% the NC remain highly transparent in visible range which is clear from absorption spectra and photograph of hexane solution of NCs (ESI, Fig. S15). When we tried to dope beyond 6% there was no much change in band gap but a little decrease of IR absorbance intensity was observed. The decrease of IR absorbance peak intensity for $ZnIn_8$ may be a result from localisation of electron charge around the cations and scattering with impurity ions.[3] Although the solid solution limit for In^{3+} in ZnO by our synthetic strategy is 8% as concluded from XRD analysis but superior plasmon property is observed up to ca. 6%.

To know details about the change of optical property upon In^{3+} doping in ZnO matrix steady state photoluminescence spectroscopy was performed. A summary of PL profile of doped and pure samples is presented in Fig.7. Normally the PL profile of ZnO based nanocrystal shows two types of emission: near band edge emission (NBE) and deep level emission (DLE). The

Nanoscale Accepted Manuscript

NBE emission which appears in UV region (nearly 375 – 378 nm) upon excitation with 330 nm for all the NCs is attributed to the radiative recombination of photo generated holes in the valence band and electrons in the conduction band i.e. the excitonic recombination. The pure ZnO NC has an intense ultra violet peak with a defect related photoluminescence peak centred at 495 nm. The green emission centred at 495 nm may be due to the (i) recombination of photo generated electrons in conduction band with the deep state defect levels (V_o, V_{Zn}, O_i, Zn_i or O_{Zn} which is situated very close to the valence band) or (ii) recombination of electron in shallow trap state (mainly Zn_i states) with the deep defects states. Where V_o and V_{Zn} stands for oxygen and Zinc vacancy respectively. O_i and Zn_i means interstitial O and Zn atom. O_{Zn} stands for oxygen atom in Zn lattice site.[52-54] It is found that the intensity of green emission peak has higher intensity than UV emitting peak for pure ZnO. XPS analysis for ZnO NC confirms (in Fig.4b) the presence of oxygen vacancy on the NCs surface and no trace of O_i (which generally appears at lower binding energy than pure O1s peak). So in pure sample only oxygen vacancy related defect states like V_o, V_o^+ or V_o^{++} are expected as the deep trap states and recombination of electron from conduction band to V_o generates the green emission. However for the doped NCs on increasing doping concentration the green emission peak decreases and high energy peaks at 398 nm, 422 nm and 449 nm become intensified. This indicates a higher band to band recombination and shallow states to valence band recombination with the consequence diminution of radiative transition due to oxygen vacancy. Also a little red shift in V_o related emission peak was observed. It indicates that In^{3+} doping in ZnO greatly affect the defect equilibrium resulting in the change in the concentration of different types of defects in ZnO NCs. From the literature it is very clear that PL peak related to O_i defects appears at higher wavelength (560 nm) than that V_o defects (500-520 nm).[55,56] The introduction of In^{3+} in ZnO matrix

Nanoscale Accepted Manuscript

promotes the oxygen diffusion in ZnO matrix[57] which leads to the suppression of oxygen vacancies (V_O) related defects and consequence creation of oxygen interstitials (O_i) defects. Thus, the presence of In^{3+} in ZnO matrix decreases the contribution of V_O related PL peak (by neutralising some of the V_o states) and increases the contribution of O_i related PL peak. The overall PL spectra are expected to show a red shift in In-doped ZnO NCs as compared to the undoped ZnO NCs. XPS analysis of O 1s peak of $ZnIn_4$ NC reveals the presence of interstitial oxygen (O_i) along with oxygen vacancy which supports our speculation regarding the presence of O_i and involvement in luminescence process. Beside the change of oxygen vacancy related PL peak intensity the other emission peaks at 397nm, 421 nm and 449 nm also get altered on changing doping percentage. The blue emission in ZnO system generally appears due to the presence of interstitial Zn atoms (Zn_i).[58] A gradual increase of doping % blue emission peak at 421 nm and 449 nm gets intensified than the band edge emission and consequence loss of green emission. The blue emission centred at 421 nm is observed for all the samples including the pure one. The overlap of band edge emission with blue emission for ZnO and $ZnIn_1$ NCs indicates that the Zn_i defect related levels are very closely situated to the bottom of conduction band. Whereas for $ZnIn_2$ to $ZnIn_6$ nanocrystal distinct nature of violet emitting and blue emitting peaks gradually appear which may be a result of increase of Zn_i concentration in the systems. The presence of Zn_i can be concluded by analysing the Zn LMM Auger peak which is often used to identify the chemical states of the zinc species.[59] Auger peaks usually show larger shape changes than XPS peaks with varying chemical states because a single Auger transition involves three electrons and many body effects. Fig. S16 shows the typical Auger Zn $L_3M_{4,5}M_{4,5}$ spectrum of the $ZnIn_4$ NC. This spectrum is Gaussian fitted with two Auger peaks centred at 494.22 eV and 496.14 eV which are attributed to the interstitial zinc (Zn_i) and Zn-O bonds respectively.

Nanoscale Accepted Manuscript

Strikingly all the PL emission intensities for the defect related emission of In doped ZnO NCs are much lower than the pure one. The appearance of surface plasmon band in doped NCs may oppose normal electron-hole recombination at the surface by reducing the separation of electron and holes within the surface depletion region.[60] Anomalous behaviour for $ZnIn_8$ NCs is found where only the UV emission is observed with total suppression of visible emission. The formation of an amorphous layer of In_2O_3 on $ZnIn_8$ NCs may responsible for this abnormal behaviour which quench the visible emission (also affects the plasmonic property of $ZnIn_8$ NCs) as it forms an insulator barrier on the NC surface.[61,62] The schematic diagram (scheme II) depicts a fair idea about the luminescence process.

For the successful practical application of the NCs, it is very necessary to deposit the NCs as a film by preserving the optical and electrical properties. In situ ligand exchange process[63] was performed to remove nonconductive organic ligand (OLAM) by formic acid. The as-prepared film was immersed in 0.1 (M) formic acid solution in acetonitrile for 5 mins. The surface of ligand exchanged film was mildly washed with ethanol and dried under vacuum. Finally the film was annealed at 300 ˚C for 2 hrs to remove the formic acid. Fig. S18a and S18b shows the cross-sectional and top view of as-deposited film of $ZnIn_4$ NCs. Whereas Fig. S18c describes the cross-section view of ligand exchanged film which shows a homogenous film formation and Fig. S18d shows the top view which gives a fair idea about the absence of cracks in the film. The films are completely transparent in the visible region (transparency ~ 95%) and the inherent surface plasmon peak remains unchanged after ligand exchange (Fig. S19). Sufficient care was taken during the ligand exchange process as excess exposure of formic acid (exposure time more than 10 mins or high concentration of formic acid) results in high decrease in surface plasmon peak intensity due to corrosion of NC's surface by formic acid.

Nanoscale Accepted Manuscript

In order to trace the conductive properties of the as annealed films, temperature dependent resistance was measured by conventional two probe method. Fig. 8 shows the variation of sheet resistance of films at temperature range 80 K to 300 K with different In^{3+} concentrations. Pure ZnO film shows relatively high room temperature (RT) sheet resistance (ρ) ~ 53.2 KΩ/sq. and a negative temperature coefficient of resistivity (TCR), characteristic of semiconductor behaviour. A clear decrease in sheet resistance of ~1.5 orders of magnitude (2 KΩ/sq.) has been observed for 1% In^{3+} doped film. Gradual increase of dopant % decreases the RT sheet resistance up to 740 Ω/sq for 6% indium doping, which reaches state of art performance of ITO colloidal coatings after annealing[64] and Ga doped ZnO coatings from colloidal inks.[5] The most interesting characteristic feature for ZIO films is that they show metal-semiconductor (MST) transition at low temperature. The MST transition temperature (T_s) varies from 250 K to 105 K with increasing In concentration. The positive value of TCR above the T_s and negative value below the T_s reflects two different conduction mechanisms are compete each other. Such behaviour in temperature dependence of resistance is common in TCO films such as Ga and Al doped ZnO,[65] Nb and La doped $SrTiO_3$[66,67] and La-doped $BaSnO_3$[68]. The decrease in sheet resistance and appearance of metal like conductivity can be explained by the increase in carrier concentration and formation of degenerate band due to In doping. Increase in n-type doping in the system gives rise to gradual filling up of the bottom state of conduction band and consequent shifting of Fermi level towards the conduction band results in the metallic behaviour.

For 2, 4 and 6% In doped films, contribution from metallic conduction process increases as the T_s shifts lower temperature. Beside the metallic conduction, below T_s the conduction process is mainly governed by variable range hopping process (VRH) in doped semiconductors. Excellent linear fit of $\ln(\rho T^{-1/2})$ *vs.* $T^{-1/4}$ plot (below T_s) supports VRH conduction process.[69] So

Nanoscale Accepted Manuscript

the In doping introduces degenerate semiconductor nature in wide band gap ZnO system which reflects metallic conductivity at room temperature. On the other hand it decreases the acceptor impurity (also confirmed from PL emission) which facile the VRH mechanism to be the predominate one. Abnormal behaviour in conductivity is found for $ZnIn_8$ film where the RT sheet resistance is higher than the other doped films, and the negative TCR value confirms the semiconductor behaviour. The dominant conduction is VRH process for $ZnIn_8$ film.

The best conductive film $ZnIn_6$ shows very low sheet resistance upon thermal annealing. Sheet resistance is dropped from 740 Ω/sq. to 120 Ω/sq. on annealing at 700 ˚C. This is the best report till date for sheet resistance of ZnO based TCO films and very close to commercially available ITO glass slide (~ 40 Ω/sq for Sigma-Aldrich, cat. No.703192). The transparency in visible region is somewhat reduced to 70% for the formation of oxygen and indium vacancies. The synthesis protocol as we discussed is very useful also for synthesizing Al^{3+} and Ga^{3+} ZnO colloids (ESI, Fig.S21) taking the dopant precursor as acetylacetonate complex. Further extensive studies regarding TCO properties of Al^{3+} and Ga^{3+} doped ZnO colloids are currently underway in our laboratory.

Conclusion:

In summary, we successfully synthesized In doped ZnO colloidal NCs by thermal decomposition of metal carboxylate salt and studied the effect of dopant source on doping percentage in host matrix. Sizes of In doped ZnO NCs decrease upon In doping which indicate that dopant impurities inhibit NC growth in solution. The effect of n-type doping in ZnO matrix on band structural change and various types of vacancy states has been thoroughly investigated from absorbance and PL spectroscopy. The doped NC shows excellent plasmonic property in near infrared region. Cost effective high quality film can be easily produced by spin casting and

Nanoscale Accepted Manuscript

in situ ligand exchange process. The doped ZnO NCs reveal metal-semiconductor transition at low temperature. The higher electrical conductivity of ZIO films concomitant with the visible range transparency and good plasmonic property makes the ZIO NCs a superior substitute of costly ITO films and a promising candidate of plasmonic materials.

Acknowledgement:

The authors Sirshendu Ghosh and Manas Saha are thankful to Council of Scientific and Industrial Research (CSIR), Govt. of India for providing the fellowship during the tenure of the work. The authors acknowledge Dr. Vishal Dev Ashok and Babusona Sarkar for their useful suggestions.

Nanoscale Accepted Manuscript

Table 1: Composition analysis of In^{3+} doped ZnO nanocrystals for different indium sources by ICP-AES and EDS analysis.

Mole (%)	In precursor	ICP-AES (mole %)	EDS (mole %)
1	$In(acac)_3$	0.92	0.79
	$In(Oac)_3$	0.45	0.37
2	$In(acac)_3$	1.74	1.68
	$In(Oac)_3$	0.78	0.72
4	$In(acac)_3$	3.56	3.28
	$In(Oac)_3$	1.24	1.08
6	$In(acac)_3$	5.42	5.29
	$In(Oac)_3$	1.85	1.78
8	$In(acac)_3$	6.94	6.72
	$In(Oac)_3$	2.14	2.10

Nanoscale Accepted Manuscript

Table 2: Optical band gap energy (E_g), plasmon wavelength (λ_p), electron concentration (N) calculated from BM effect and Mie's theory for ZnO nanocrystals with different In doping contents.

Doping (%)	E_g [eV]	λ_p (nm)	N [cm^{-3}] X10^{19} (Burstein–Mass effect)	N [cm^{-3}] X10^{19} (Mie's theory)
ZnO (0%)	3.395	—	—	—
$ZnIn_1O$ (1%)	3.438	5662.514	0.455	6.491
$ZnIn_2O$ (2%)	3.497	4955.401	1.220	8.476
$ZnIn_4O$ (4%)	3.562	4741.583	2.556	9.222
$ZnIn_6O$ (6%)	3.576	4323.389	2.923	11.092
$ZnIn_8O$ (8%)	3.565	3838.771	2.630	14.069

Nanoscale Accepted Manuscript

References:

(1) Ginley, D. S.; Hosono, H.; Paine, D. C. *Handbook of Transparent Conductors;* Springer: New York, 2010.

(2) Wan, Q.; Dattoli, E. N.; Lu, W. *Appl. Phys. Lett*. **2007**, *90*, 222107.

(3) Wang, T.; Radovanovic P. V. *J. Phys. Chem. C* **2011**, *115*, 406–413.

(4) Buonsanti, R.; Llordes, A.; Aloni, S.; Helms, B. A.; Milliron, D. J. *Nano Lett.* **2011**, *11*, 4706–4710.

(5) Gaspera, E. D.; Bersani, M.; Cittadini, M.; Guglielmi, M.; Pagani, D.; Noriega, R.; Mehra, S.; Salleo, A.; Martucci, A. *J. Am. Chem. Soc.* **2013**, *135*, 3439−3448.

(6) Serin, T.; Yildiz, A.; Uzun, Ş.; Çam, E.; Serin, N. *Phys. Scr.* **2011,** *84*, 065703 (6pp).

(7) Gordon, T. R.; Paik, T.; Klein, D. R.; Naik, G. V.; Caglayan, H.; Boltasseva, A.; Murray, C. B. *Nano Lett.* **2013**, *13*, 2857−2863.

(8) Trizio, L. D.; Buonsanti, R.; Schimpf, A. M.; Llordes, A.; Gamelin, D. R.; Simonutti, R.; Milliron, D. J. *Chem. Mater.* **2013**, *25*, 3383−3390.

(9) Nozik, A. J. *Phys. Rev. B* **1972**, *6*, 453−459.

(10) Coutts, T. J.; Young, D. L.; Li, X.; Mulligan, W. P.; Wu, X. *J. Vac. Sci. Technol. A* **2000**, *18*, 2646−2646.

(11) Wang, A.; Babcock, J. R.; Edleman, N. L.; Metz, A. W.; Lane, M. A.; Asahi, R.; Dravid, V. P.; Kannewurf, C. R.; Freeman, A. J.; Marks, T. J. *Proc. Natl. Acad. Sci.* **2001**, *98*, 7113−6.

(12) Bhosle, V.; Narayan, J. *J. Appl. Phys.* **2006**, *100*, 093519.

(13) Hwang, D-K.; Oh, M-S.; Lim, J-H.; Park, S-J. *J. Phys. D: Appl. Phys.* **2007**, *40*, R387–R412.

Nanoscale Accepted Manuscript

(14) Li, L.; Hutter, T.; Finnemore, A. S.; Huang, F. M.; Baumberg, J. J.; Elliott, S. R.; Steiner, U.; Mahajan, S. *Nano Lett*. **2012**, *12*, 4242−4246.

(15) Kumar, V.; Singh, R.G.; Purohit, L.P.; Mehra, R.M. *J. Mater. Sci. Technol.* **2011**, *27*, 481–488.

(16) Fang, T-H.; Kang, S-H. *Curr. Appl. Phys.* **2010**, *10*, 1076–1086.

(17) Li, D. P.; Wang, G. Z.; Han, X. H. *J. Phys. D: Appl. Phys.* **2009**, *42*, 175308.

(18) Wang, Z. L.; Kong, X.Y.; Zuo, J. M. *Phys Rev Lett.* **2003**, *91*, 185502.

(19) Wang, Z. L. *J. Phys.: Condens. Matter* **2004**, *16*, R829–R858.

(20) Yang, M.; Sun, K.; Kotov, N. A. *J. Am. Chem. Soc*. **2010**, *132*, 1860–1872.

(21) Xu, L.; Guo, Y.; Liao, Q.; Zhang, J.; Xu, D. *J. Phys. Chem. B* **2005**, *109*, 13519-13522.

(22) Meyer, B.; Marx, D. *Phys. Rev. B* **2003**, *67*, 035403.

(23) Wang, Z. L.; Kong, X. Y.; Ding, Y.; Gao, P. X.; Hughes, W. L.; Yang, R. S.; Zhang, Y. *Adv. Funct. Mater.* **2004**, *14*, 943.

(24) Yang, R. S.; Ding, Y.; Wang, Z. L. *Nano Lett.* **2004**, *4*, 1309.

(25) Shukla, N.; Liu, C.; Jones, P. M.; Weller, D. *J. Magn. Magn. Mater.* **2003**, *266*, 178.

(26) Bahers, T. L.; Pauporté, T.; Labat, F.; Lefevre, G.; Ciofini, I. *Langmuir* **2011**, *27*, 3442–3450.

(27) Schwartz, D. A.; Norberg, N. S.; Nguyen, Q. P.; Parker, J. M.; Gamelin, D. R. *J. Am. Chem. Soc.***2003,** *125*, 13205.

(28) Farvid, S. S.; Dave, N.; Wang, T.; Radovanovic, P. V. *J. Phys. Chem. C* **2009,***113*,15928

(29) Feng, J.; Zhu, H.; Yang, X. *Nanoscale* **2013**, *5*,6318.

(30) Erwin, S. C.; Zu, L.; Haftel, M. I.; Efros, A. L.; Kennedy, T. A.; Norris, D. J. *Nature* **2005**, *436*, 91.

Nanoscale Accepted Manuscript

(31) Oxtoby, D. W.; *Acc. Chem. Res.*, **1998**, *31 (2)*, 91.

(32) Crist, P. D. B. V. Handbook of The Elements and Native Oxides(XPS International, Inc., 1999), *Vols. 1 and 2*.

(33) Ilyas, U.; Rawat, R. S.; Tan, T. L.; Lee, P.; Chen, R.; Sun, H. D.; Fengji, L.; Zhang, S. *J. Appl. Phys* **2012,** *111*, 033503.

(34) Tay, Y. Y.; Li, S.; Sun, C. Q.; Chen, P. *Appl. Phys. Lett.* **2006,** *88*, 173118.

(35) Ghosh, S.; Das, K.; Sinha, G.; Lahtinen, J.; De, S. K. *J. Mater. Chem. C* **2013**, *1*, 5557–5566.

(36) Liu, W.; Li, W.; Hu, Z.; Tang, Z.; Tang, X. *Appl. Phys. Lett.* **2011,** *110*, 013901.

(37) Sarath Kumar, S. R.; Hedhili, M. N.; Alshareef, H. N.; Kasiviswanathan, S. *Appl. Phys. Lett.* **2010**, *97*, 111909.

(38) Fox, M. *Optical Properties of Solids*; Oxford University Press: NewYork, 2001.

(39) Mulvaney, P.; Liz-Marzan, L. M.; Giersig, M.; Ung, T. *J. Mater. Chem*. **2000**, *10*, 1259−1270.

(40) Kanehara, M.; Koike, H.; Yoshinaga, T.; Teranishi, T. *J. Am. Chem. Soc.* **2009**, *131*, 17736–17737.

(41) Baer, W. S. *Phys. Rev.***1967**, *154*, 785.

(42) Lin, W.; Ding, K.; Lin, Z.; Zhang, J.; Huang, J.; Huang, F. *CrystEngComm*, **2011**, *13*, 3338–334.

(43) Hammarberg, E.; Prodi-Schwab, A.; Feldmann, C. *J. Coll. Int. Sc.***2009,** 334, 29.

(44) Ellingson, R. J.; Beard, M. C.; Johnson, J. C.; Yu, P.; Micic, O. I.; Nozik, A. J.; Shabaev, A.; Efros, A. L. *Nano Lett.* **2005**, *5*, 865–871.

(45) Mridha, S.; Basak, D. *J. Phys. D: Appl. Phys.* **2007**, *40*, 6902–6907.

Nanoscale Accepted Manuscript

(46) Lu, J. G.; Fujita, S.; Kawaharamura, T.; Nishinaka, H.; Kamada, Y.; Ohshima, T.; Ye, Z. Z.; Zeng, Y. J.; Zhang, Y. Z.; Zhu, L. P.; He, H. P.; Zhao, B. H. *J. Appl. Phys.* **2007**, *101*, 083705.

(47) Suwanboon, S.; Amornpitoksuk, P.; Haidoux, A.; Tedenac, J. C.*J. Alloys Compd.* **2008**, *462*, 335–339.

(48) Sernelius, B.; Berggren, K. F.; Jin, Z. C.; Hamberg, I.; Granqvist, C. *Phys. Rev. B* **1988**, *37*, 10244–10248.

(49) Chen, R.; Zhu, P.; Zhao, T.; Fu, X.; Zhou, F.; Sun, R. *Eur. J. Inorg. Chem.* **2013**, *20,* 3491–3496.

(50) Sans, J. A.; Sánchez-Royo, J. F.; Segura, A.; Tobias, G.; Canadell, E. *Phys. Rev B* **2009**, *79*,195105.

(51) Jia, J.; Takasaki, A.; Oka, N.; Shigesatoa, Y. *J. Appl. Phys.***2012,** *112*, 013718.

(52) Wena, F.; Li, W.; Moona, J-H.; Kim, J. H. *Solid State Communications* **2005,** *135*, 34.

(53) Vanheusden, K.; Warren, W. L.; Seager, C. H.; Tallant, D. R.; Voigt, J. A. *J. Appl. Phys.***1996**, *79*, 7983.

(54) Shi, Y.L.; Wang, J.; Li, H.L. *Appl. Phys. A* **2004,** *79*, 1797.

(55) Kurbanov, S.S.; Panin, G.N.; Kim, T.W.; Kang, T.W. *J. Lumin.* **2009**, *129*, 1099.

(56) Hsu, J.W.P.; Tallant, D.R.; Simpson, R.L.; Missert, N.A.; Copeland, R.G. *Appl. Phys. Lett.* **2006**, *88*, 252103.

(57) Ryoken, H.; Sakaguchi, I.; Ohashi, N.; Sekiguchi, T.; Hishita, S.; Haneda, H. *J. Mater. Res.***2005**, *20*, 2866.

(58) Zeng, H.; Duan, G.; Li, Y.; Yang, S.; Xu, X.; Cai, W. *Adv. Funct. Mater.* **2010**, *20*, 561–572.

(59) Wolan, J. T.; Horflund, G. B. *Appl. Surf. Sci.***1998**, *125*, 251.

Nanoscale Accepted Manuscript

(60) Cheng, C. W.; Sie, E. J.; Liu, B.; Huan, C. H. A.; Sum, T. C. *Appl. Phys. Lett.* **2010**, *96*, 071107.

(61) Richters, J-P.; Voss, T.; Kim, D S.; Scholz, R.; Zacharias, M. *Nanotechnology* **2008**, *19*, 305202.

(62) Richters, J-P.; Voss, T.; Wischmeier, L.; Rückmann, I.; Gutowski, J. *Appl. Phys. Lett.* **2008**, *92*, 011103.

(63) Zarghami, M. H.; Liu, Y.; Gibbs, M.; Gebremichael, E.; Webster, C.; Law, M. *ACS Nano* **2010**, *4*, 2475–2585.

(64) Lee, J.; Lee, S.; Li, G.; Petruska, M. A.; Paine, D. C.; Sun, S. *J. Am. Chem. Soc.* **2012**, *134*, 13410−13414.

(65) Han, J. P.; Mantas, P. Q.; Senos, A. M. R. in 7th International Conference on Electronic Ceramics and Their Applications (ELECTROCERAMICS VII-2000)(Elsevier Science Ltd, Portoroz, Slovenia, 2000), p. 1883.

(66) Ramadan, W.; Ogale, S. B.; Dhar, S.; Zhang, S. X.; Kundaliya, D. C.; Satoh, I.; Venkatesan, T. *Appl. Phys. Lett.***2006**, *88*, 142903.

(67) Cho, J. H.; Cho, H. J. *Appl. Phys. Lett.* **2001,** *79*, 1426.

(68) Liu, Q.; Liu, J.; Li, B.; Li, H.; Zhu, G. *Appl. Phys. Lett* **2012**, *101*, 241901.

(69) Mott, N. F.; Davis, E. A. Electronic processes in non-crystalline materials, 2nd ed. (clarendon, oxford, 1979).

Nanoscale Accepted Manuscript

Figure captions:

Fig. 1. (a) XRD patterns of pure and doped ZnO nanocrystals $ZnIn_1$, $ZnIn_2$, $ZnIn_4$, $ZnIn_6$ and $ZnIn_8$. (b) change of lattice parameter and strain with In doping.

Fig. 2. (a) FESEM image of pure ZnO.(b) Low resolution TEM image of pure ZnO nanopyramid. The top-left and bottom right insets of Figure depicts the tilted ($X = 41.1°$, $Y = 0°$) and side views of a single ZnO hexagonal nanopyramid. (c) SAED pattern of nanopyramid. (d) A single hexagonal pyramid viewed from (0001) zone axis. (e) SAED pattern of single nanocrystal. (f) Schematic presentation of a nanopyramid. (g) HRTEM image of a nanocrystal at the cross-section of two edge of base. Inset shows the corresponding FFT pattern of the area. (h) Side view of a nanopyramid. (i) HRTEM image of tip of pyramid. (j) HRTEM image of base of pyramid.

Fig. 3. STEM dark field image and EDS element mapping of Zn, In and O.

Fig. 4. XPS spectra of (a, b) the pure and $ZnIn_4$ samples for Zn 2p and O 1s peaks respectively; (c) the In 3d peaks for $ZnIn_4$ sample.

Fig. 5. Optical absorbance of all ZnIn samples in Vis-NIR region normalised with respect to band gap absorbance.

Fig. 6. FTIR spectra of ZnIn samples in solid form with different amount In loding. The extra sharper peaks is due to the organic ligand absorbed on nanocrystal's surface.

Fig. 7. PL profile of ZnIn samples at different In concentration.

Fig. 8. Temperature dependent sheet resistance of (a) pure ZnO, (b) $ZnIn_1$, (c) $ZnIn_2$, (d) $ZnIn_4$, (e) $ZnIn_6$ and (f) $ZnIn_8$.

Scheme I: shape transformation of ZnIn nanocrystals on increasing In loading.

Nanoscale Accepted Manuscript

Scheme II: Schematic presentation of band structure and interstitial defects of (A) pure ZnO, (B) ZnO at moderate doping concentration (2, 4 and 6 mole%), (C) $ZnIn_8$ sample; E_{LS} is the localised state due to excess In^{3+} and $E_{LS}{}^{/}$ is the deformed localised state (LS) after interaction with conduction band (E_c). E_F is flattened conduction band after interaction with LS.

.

Nanoscale Accepted Manuscript

Figures:

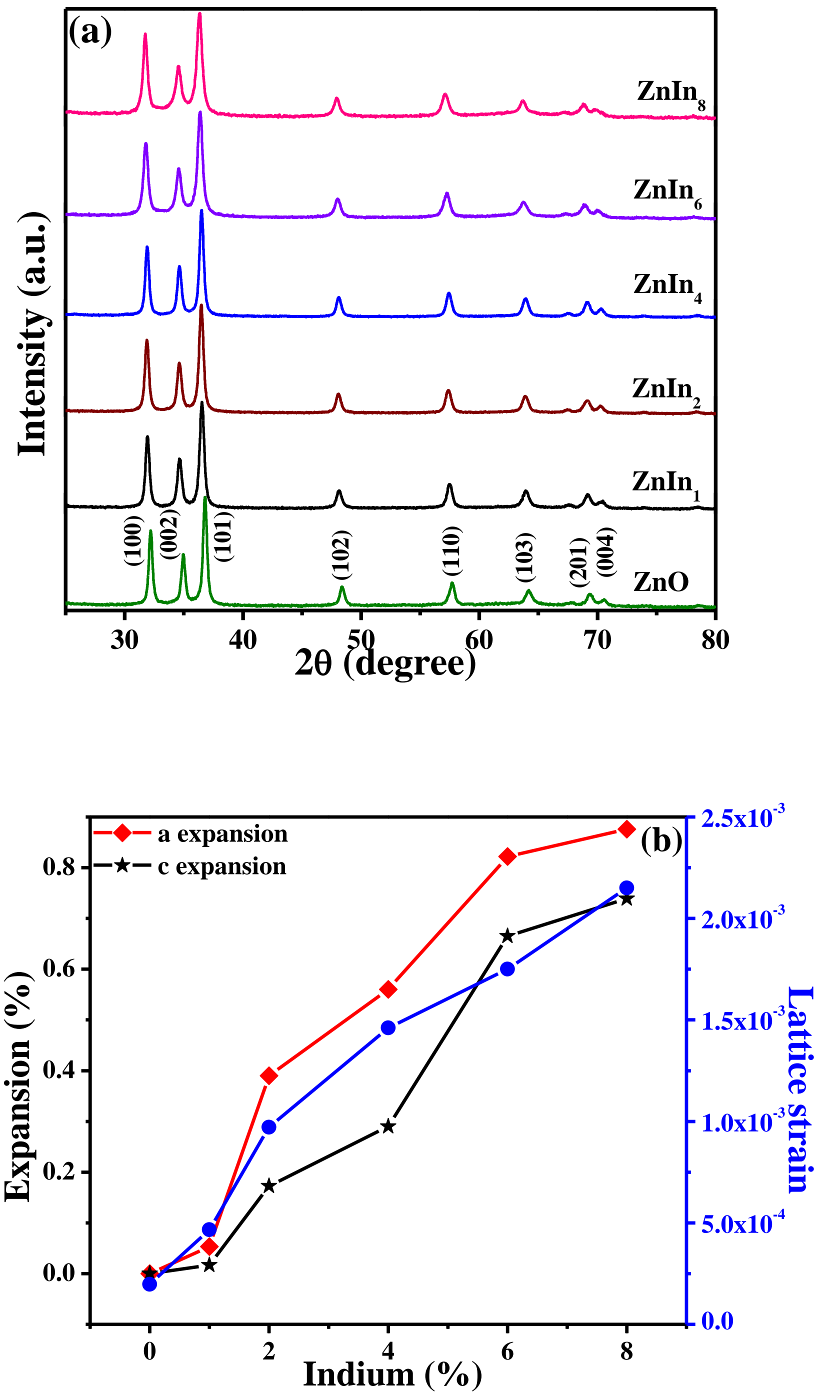

Fig. 1

Nanoscale Accepted Manuscript

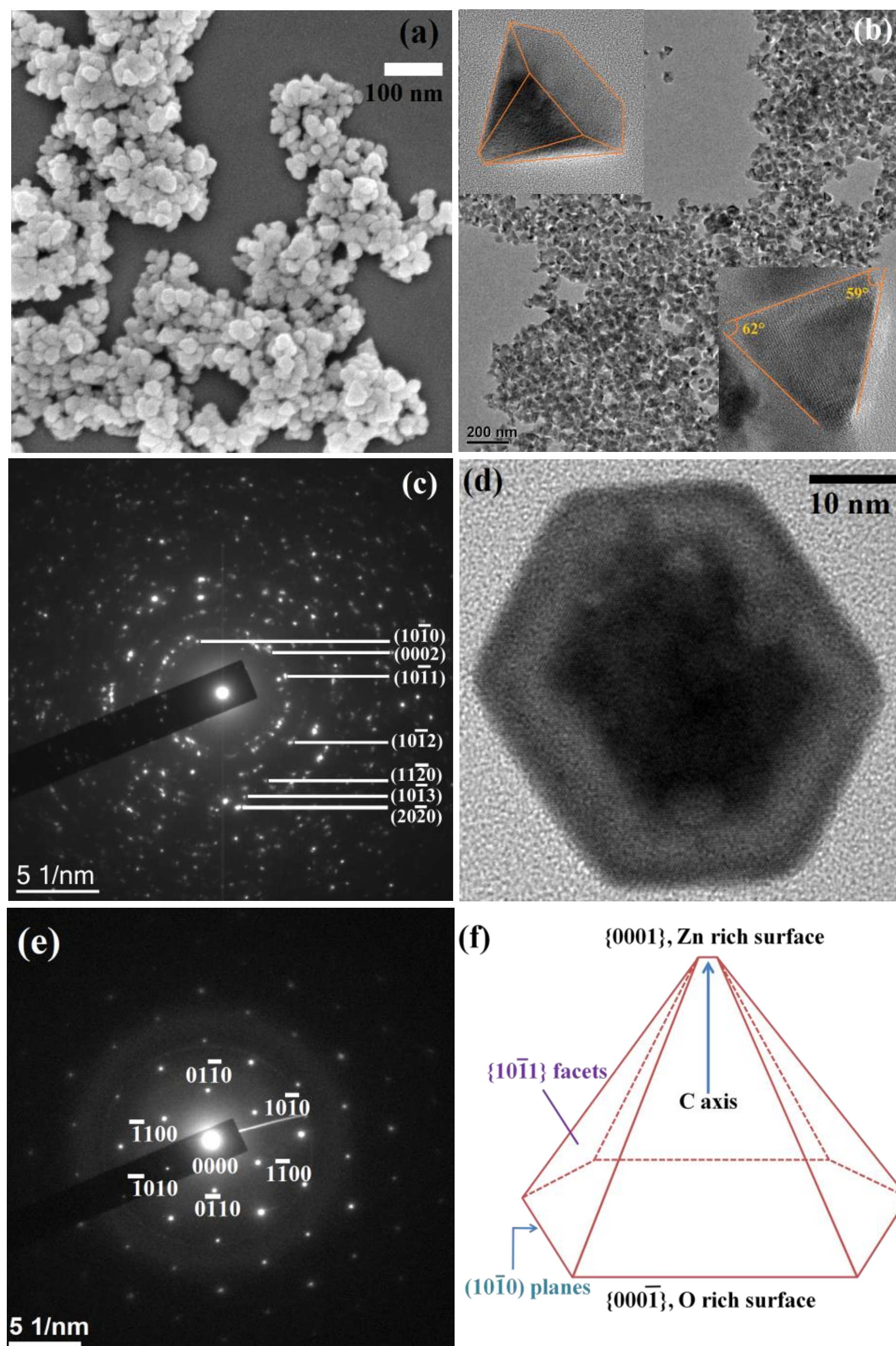

Fig. 2

Nanoscale Accepted Manuscript

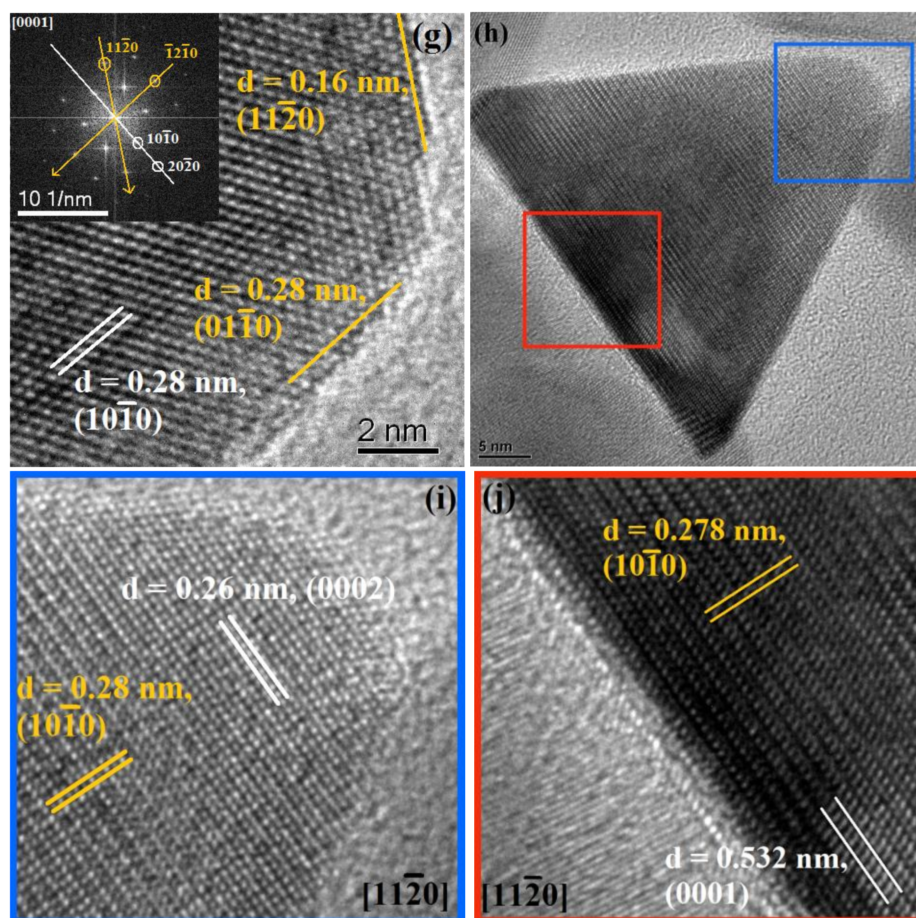

Fig. 2

Nanoscale Accepted Manuscript

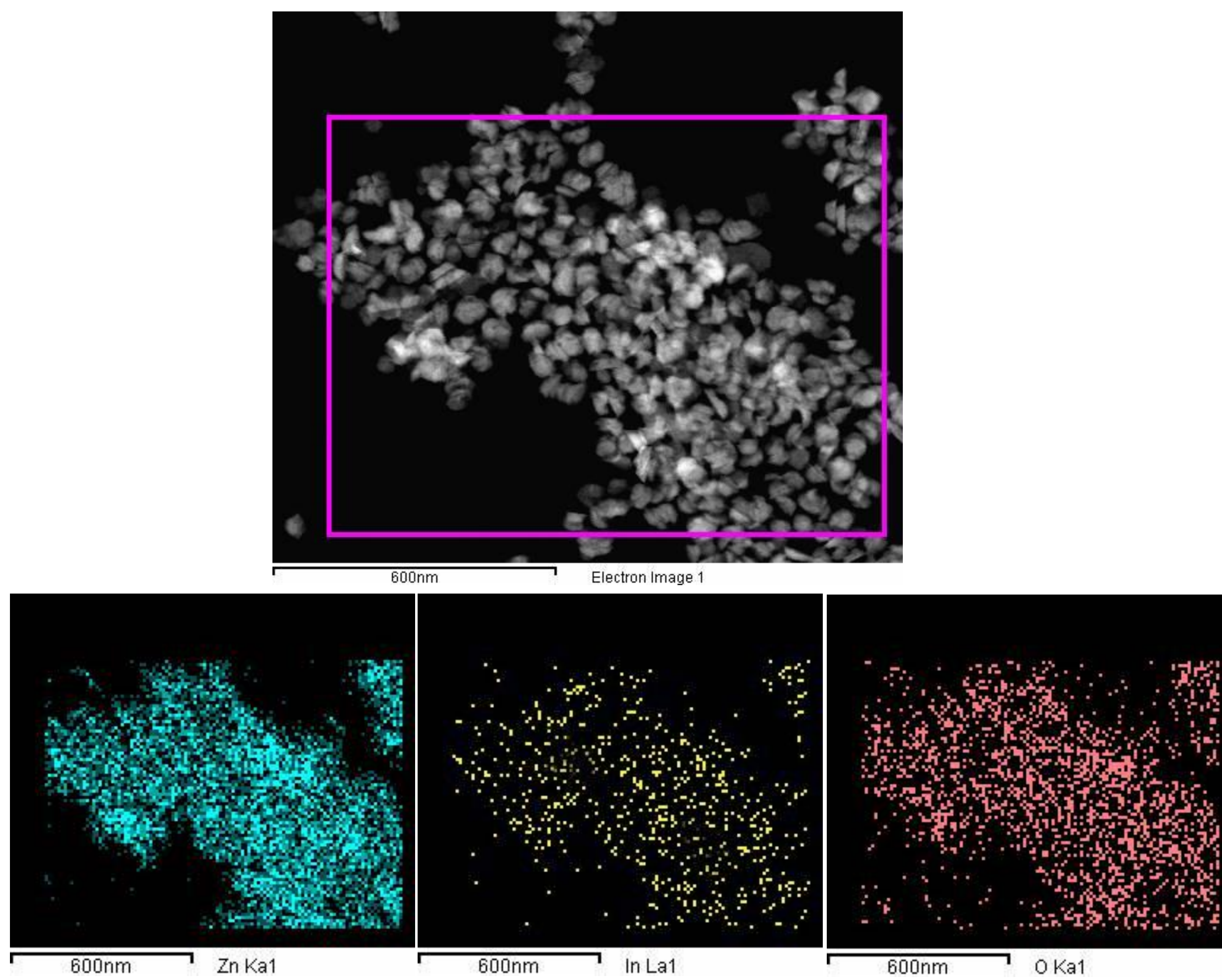

Fig. 3

Nanoscale Accepted Manuscript

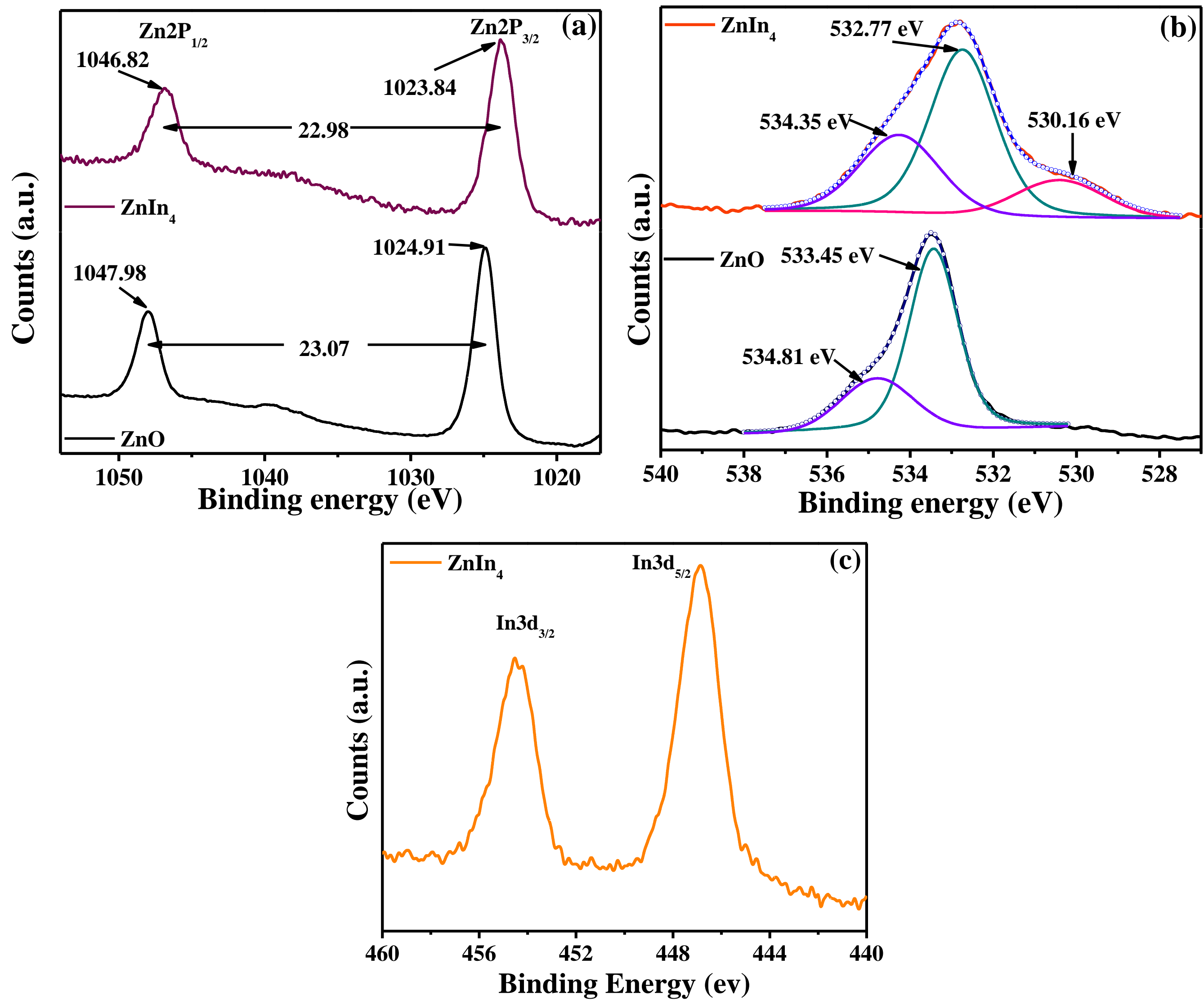

Fig. 4

Nanoscale Accepted Manuscript

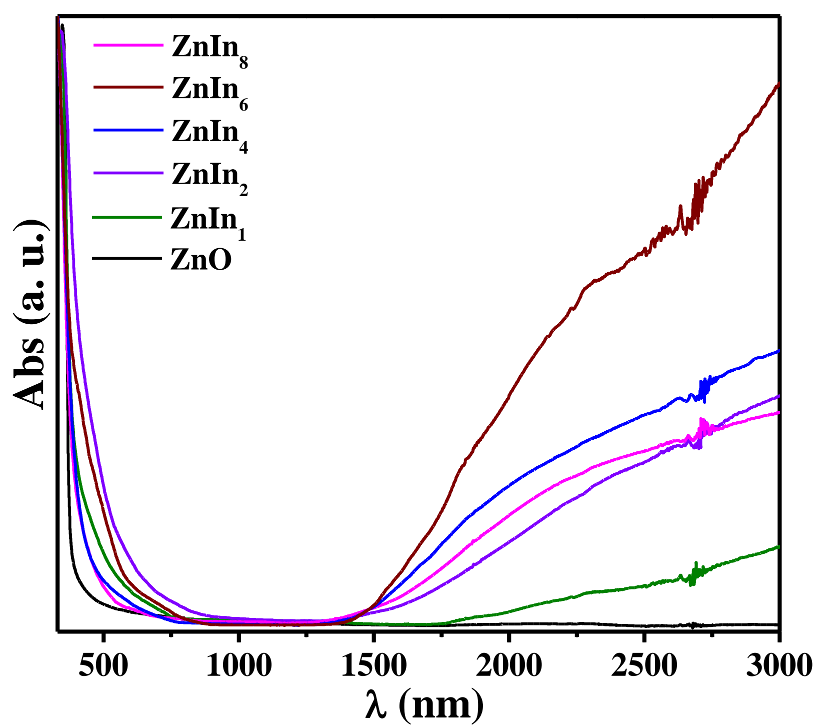

Fig. 5

Nanoscale Accepted Manuscript

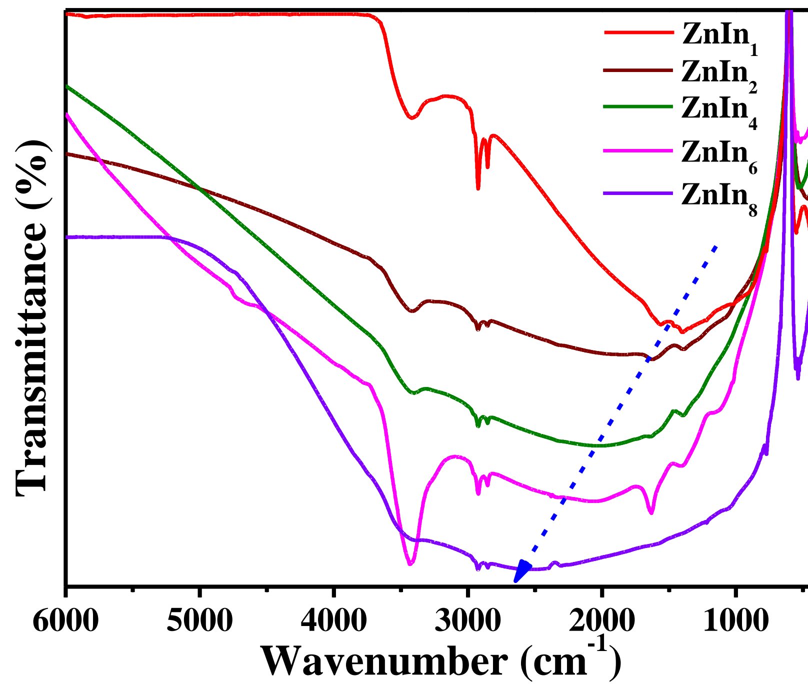

Fig. 6

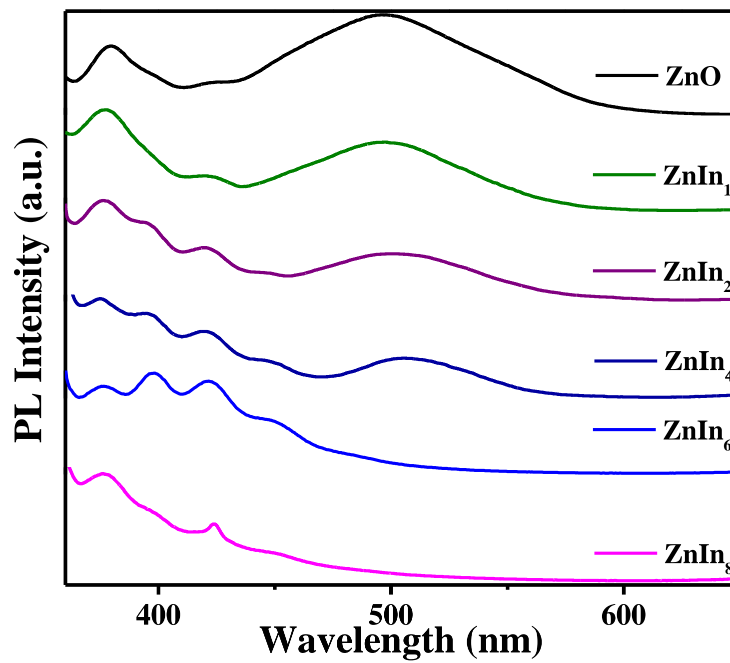

Fig. 7

Nanoscale Accepted Manuscript

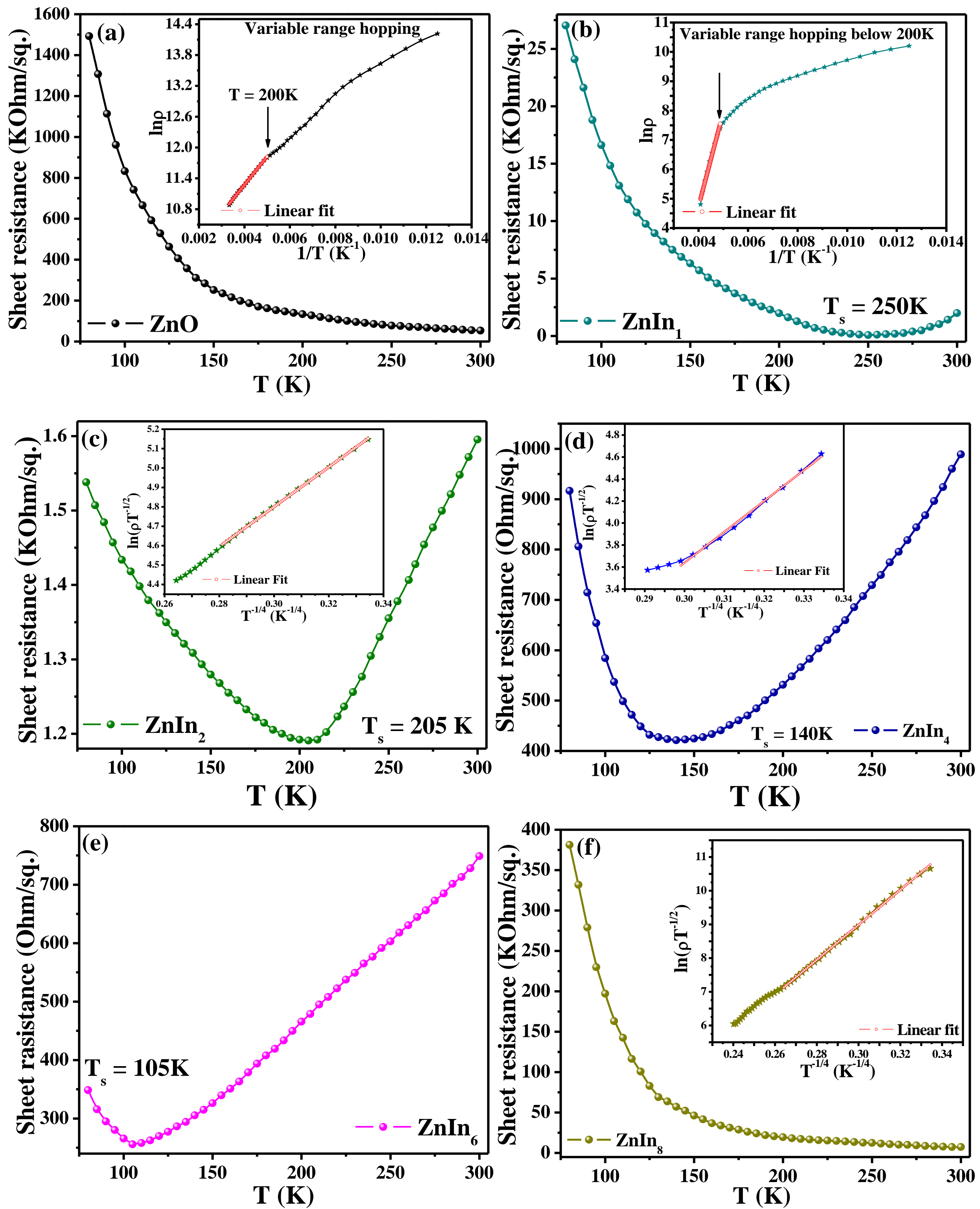

Fig. 8

Nanoscale Accepted Manuscript

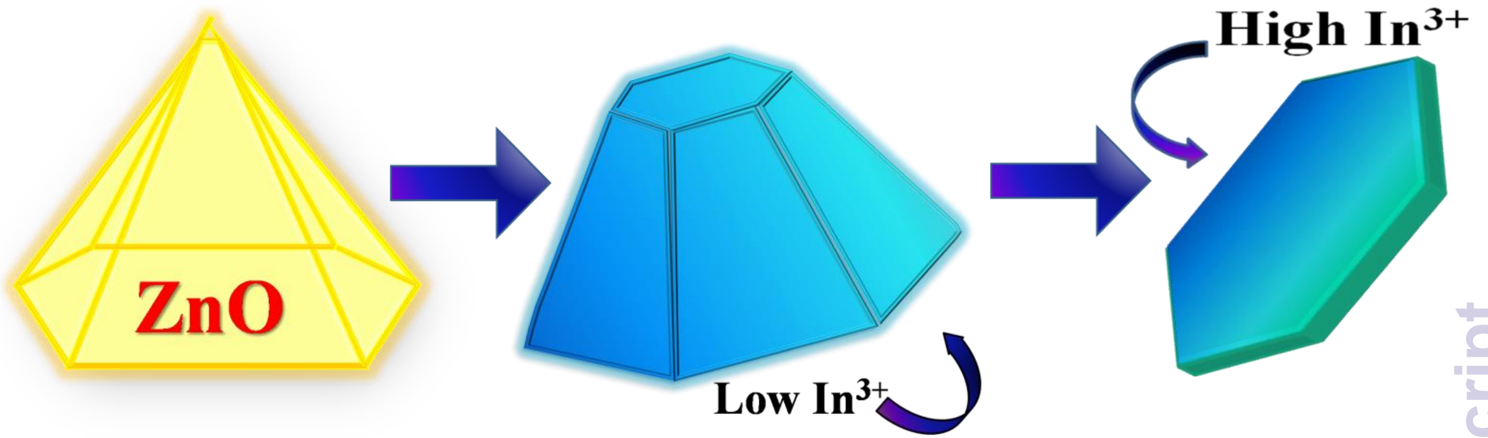

Scheme-I

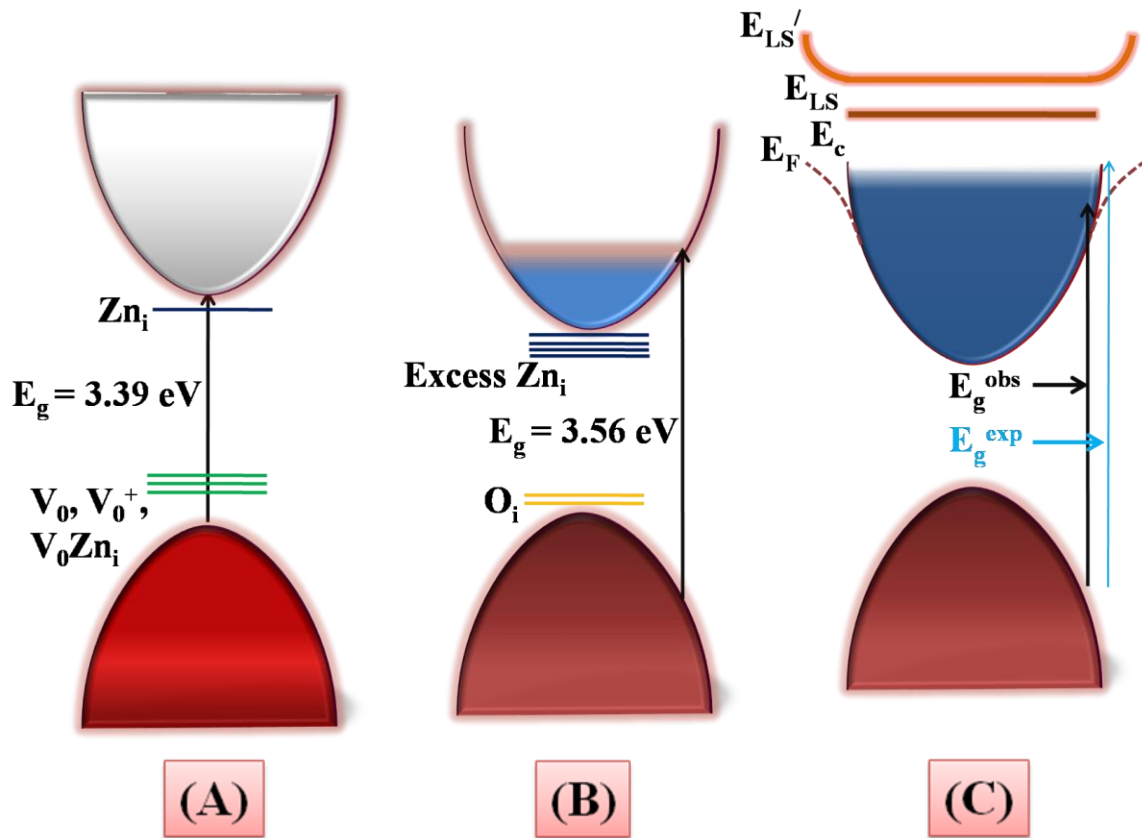

Scheme - II

Nanoscale Accepted Manuscript